Physical Properties of Transneptunian Objects

D. P. Cruikshank
NASA Ames Research Center

M. A. Barucci
Observatoire de Paris, Meudon

J. P. Emery
SETI Institute and NASA Ames Research Center

Y. R. Fernández
University of Central Florida

W. M. Grundy
Lowell Observatory

K. S. Noll
Space Telescope Science Institute

J. A. Stansberry
University of Arizona

In 1992, the first body beyond Neptune since the discovery of Pluto in 1930 was found. Since then, nearly a thousand solid bodies, including some of planetary size, have been discovered in the outer solar system, largely beyond Neptune. Observational studies of an expanding number of these objects with space- and groundbased telescopes are revealing an unexpected diversity in their physical characteristics. Their colors range from neutral to very red, revealing diversity in their intrinsic surface compositions and/or different degrees of processing that they have endured. While some show no diagnostic spectral bands, others have surface deposits of ices of H_2O, CH_4, and N_2, sharing these properties with Pluto and Triton. Thermal emission spectra of some suggest the presence of silicate minerals. Measurements of thermal emission allow determinations of the dimensions and surface albedos of the larger (diameter > ~75 km) members of the known population; geometric albedos range widely from 2.5% to >60%. Some 22 transneptunian objects (including Pluto) are multiple systems. Pluto has three satellites, while 21 other bodies, representing about 11% of the sample investigated, are binary systems. In one binary system where both the mass and radius are reliably known, the mean density of the primary is ~500 kg/m^3, comparable to some comets [e.g., Comet 1P/Halley (*Keller et al.,* 2004)].

1. INTRODUCTION

The many objects found orbiting the Sun beyond Neptune, beginning with the first discovery in 1992 (*Jewitt and Luu,* 1993), open a new window on the content, dynamics, origin, and evolution of our own solar system, and give rich insights into those same aspects of protoplanetary disks and extrasolar planetary systems. Our present understanding of the population of transneptunian objects is significantly greater than our understanding of the asteroid belt was at the time when a comparable number of asteroids were known (early 1920s). This improvement arises from the fact that, in contrast with the development of asteroid science, we are studying the distant transneptunian objects with the full range of available observational techniques in parallel rather than in a serial way. By bringing together dynamical studies of their orbits and photometric, spectroscopic, and radiometric observations, we are rapidly gaining insight into the origin of transneptunian objects and their relationship to the solar nebula and protoplanetary disks around young or forming stars.

This chapter is focused on the physical properties of the objects beyond Neptune derived from observational studies with Earth- and spacebased telescopes. Those physical properties include dimensions, surface compositions, colors, and a taxonomy derived from that information, the occurrence of binary systems, and in exceptional cases masses and mean densities.

The objects with perihelia beyond Neptune, which as of early 2006 some 900 were known, have received many designations and names, both formal and informal. Three distinct dynamical populations have become apparent as the discoveries continue. The first grouping, which includes the majority of the objects discovered to date, is known as the *classical Kuiper belt*. It consists of objects in near circular orbits with semimajor axes around 45 AU. These orbits are stable against Neptune's perturbations over the age of the solar system. The second population consists of objects in orbits with 2:3 resonance with Neptune, as in the case of Pluto. These objects are informally referenced by their etymologically grotesque name, *"Plutinos."* Taken together, these two populations are frequently referred to as Kuiper belt objects (KBOs), a term that is used in this paper. The third population consists of objects in highly eccentric orbits with perihelia generally within the classical Kuiper belt (although some are inside Neptune's orbit), but with aphelia far outside. These bodies have been dynamically excited by Neptune; they are called *scattered disk* objects. In this chapter we refer to all of them with the most general term, *transneptunian objects,* or TNOs, but where it is useful to discuss dynamical categories, we use the generally accepted terms, resonant and nonresonant Kuiper belt objects (KBOs) and scattered disk objects (see chapter by Chiang et al.). An additional class, the Centaurs, consists of objects derived from the TNO population and occupying temporary orbits that cross those of the major planets. About 80 such objects having perihelia <30 AU are known as of early 2006.

In this review we will find it useful to include the planet Pluto, Neptune's satellite Triton, and the Centaurs; in discussing spectroscopy in the thermal spectral region ($\lambda >$ 10 μm), we also include the jovian Trojan asteroids for comparison. Pluto shares physical characteristics with some of the more recently discovered objects in the transneptunian region (e.g., *Owen et al.,* 1993; *Douté et al.,* 1999), while Triton has similar physical characteristics to Pluto (e.g., *Cruikshank et al.,* 1993; *Quirico et al.,* 1999) and is widely thought to have been captured into a retrograde orbit by Neptune from the TNO population (e.g., *McKinnon et al.,* 1995). The jovian Trojans are a family of small bodies that share more characteristics with comets and Centaurs than with main-belt asteroids (*Emery et al.,* 2006), and probably originated in the outer solar system.

2. COLORS AND TAXONOMY

Observations of brightness and color in the extended visible spectral region (0.3–1.0 μm) have been obtained for a large sampling of TNOs, and photometric observations in several colors obtained in recent years have yielded high quality B, V, R, and I measurements for more than 130 objects (see *Barucci et al.,* 2005a, for complete references). These observations reveal a clear diversity in color among the TNO population, noted early in the investigation of these objects (*Luu and Jewitt,* 1996). Relevant statistical analyses have been performed and a wide range of correlations between optical colors and orbital parameters have been analyzed (*Tegler and Romanishin,* 2000, 2003; *Doressoundiram et al.,* 2002; *Trujillo and Brown,* 2002; *Tegler et al.,* 2003; *Peixhino et al.,* 2004; *Doressoundiram et al.,* 2005a). Color variation is an important diagnostic of diversity in surface composition and the evolution of surface composition and microstructure through processing by various physical processes, a subject to which we return below.

When dealing with a large number of objects it is useful to distinguish groups of objects with similar surface properties. *Barucci et al.* (2005a) applied the multivariate statistic analysis (G mode) (*Barucci et al.,* 1987) to the TNO and Centaur populations; this and the principal component analysis are the same techniques used in the 1980s to classify the asteroid population (*Tholen,* 1984; *Tholen and Barucci,* 1989).

Barucci et al. (2005a), considering all the high-quality available colors on TNOs and Centaurs published after 1996, analyzed (1) a set of data for 135 objects observed in the B, V, R, and I bands; (2) a set of 51 objects observed in the B, V, R, I, and J bands with high-quality homogeneous data; and (3) a subsample of 37 objects that also included H-band measurements. They selected as a primary sample for the analysis a complete and homogeneous set of 51 objects observed in five filters (B, V, R, I, J), adopting the mean values weighted with the inverse of the error of individual measurement when multiple observations of an object were available.

The results of the analyses show the presence of four groups where J color plays the main role in discriminating the groups (J weight is 46%). The four homogeneous groups showing a high confidence level (corresponding to 3s) have been named BB, BR, IR, and RR. The same well-determined four groups were found when the analysis was applied to a subset of 37 objects for which the H color was also available.

In Table 1, the color average value and the standard deviation for each group are given. The BB (blue) group consists of objects having neutral colors with respect to the Sun, while the RR group has a very strong red color. The BR group includes objects with an intermediate blue-red color, while the IR group includes moderately red objects.

The G mode can be extended (*Fulchignoni et al.,* 2000) to assign objects for which the same set of variables become available to one of the already defined taxonomic groups, even if only a subset of variables used in the initial taxonomy is known for new objects. Such an extension has been applied to the 84 other TNOs for which only B, V, R, and I colors were available, and an indication of the classification has been obtained for 69 objects.

The investigation of the diversity among the TNOs can help in understanding their characteristics and the different physical processes that have affected their surfaces. The four groups noted here are well defined and homogeneous in color properties. To better understand the surface composition properties of each group, we have superimposed representative compositional surface models calculated for some of the well-studied objects (Fig. 1). We return below

TABLE 1. Average colors and the relative standard deviation for the four taxonomic groups obtained by G-mode analysis on the sample of 51 objects (V-H has been computed for a subset of 37 objects).

Class	B-V	V-R	V-I	V-J	V-H
BB	0.70 ± 0.04	0.39 ± 0.03	0.77 ± 0.05	1.16 ± 1.17	1.21 ± 0.52
BR	0.76 ± 0.06	0.49 ± 0.03	0.9 ± 0.07	1.67 ± 0.19	2.04 ± 0.24
IR	0.92 ± 0.03	0.61 ± 0.03	1.20 ± 0.04	1.88 ± 0.09	2.21 ± 0.06
RR	1.08 ± 0.08	0.71 ± 0.04	1.37 ± 0.09	2.27 ± 0.20	2.70 ± 0.24

to questions of the efficacy and uniqueness of compositional models of planetary bodies.

3. SPECTROSCOPY (0.3–5 MICROMETERS)

3.1. Visible and Near-Infrared Spectral Region

While broadband colors provide useful information on the surfaces of these objects, spectroscopy is the only way to investigate their surface compositions in detail. Although the faintness of these objects limits spectroscopic observations, the use of some of the world's largest telescopes has yielded combined visible region and infrared spectra for about 20 objects.

The visible region spectra are generally featureless, but show differences in the spectral slope consistent with multicolor photometry. Three objects show possible broad absorptions in their spectra; 47932 (2000 GN_{171}) shows an absorption band centered near 0.7 μm, while the spectrum of 38628 (2000 EB_{173}) suggests two weak features centered at 0.6 μm and at 0.745 μm (*Lazzarin et al.,* 2003; *de Bergh et al.,* 2004). The spectrum of 2003 AZ_{84} (*Fornasier et al.,* 2004a) also seems to show a weak absorption centered near 0.7 μm. These features are very similar to those due to aqueously altered minerals, as found in some main-belt asteroids (*Vilas and Gaffey,* 1989). We note further that hydrated silicates are a dominant component of carbonaceous meteorites. *Jewitt and Luu* (2001) have reported absorption bands (around 1.4, 1.9 μm) of phyllosilicates in the spectrum of the Centaur 26375 1999 DE_9. All these features are rather weak, and require confirmation.

Finding aqueous altered materials in TNOs would not be too surprising (*de Bergh et al.,* 2004) since hydrous silicates are detected in interplanetary dust particles (IDPs) and micrometeorites, and by inference will be found in comets. In experiments with the condensation of magnesiosilica smokes in the presence of water, *Reitmeijer et al.* (2004) produced protophyllosilicates in an environment that may be similar to that in stellar outflows and the inner regions of the solar nebula. Their results may have implications for the pervasiveness of hydrated amorphous protophyllosilicates in comets, and by association, icy protoplanets like TNOs.

While broad spectral coverage of the visible and near-infrared region is a necessary condition to allow a diagnosis for silicate minerals, carbonaceous assemblages, organics, and ices and/or hydrocarbons, in some cases it is not a sufficient condition. Some objects exhibit no discrete absorption bands, in which case the analysis can use only color

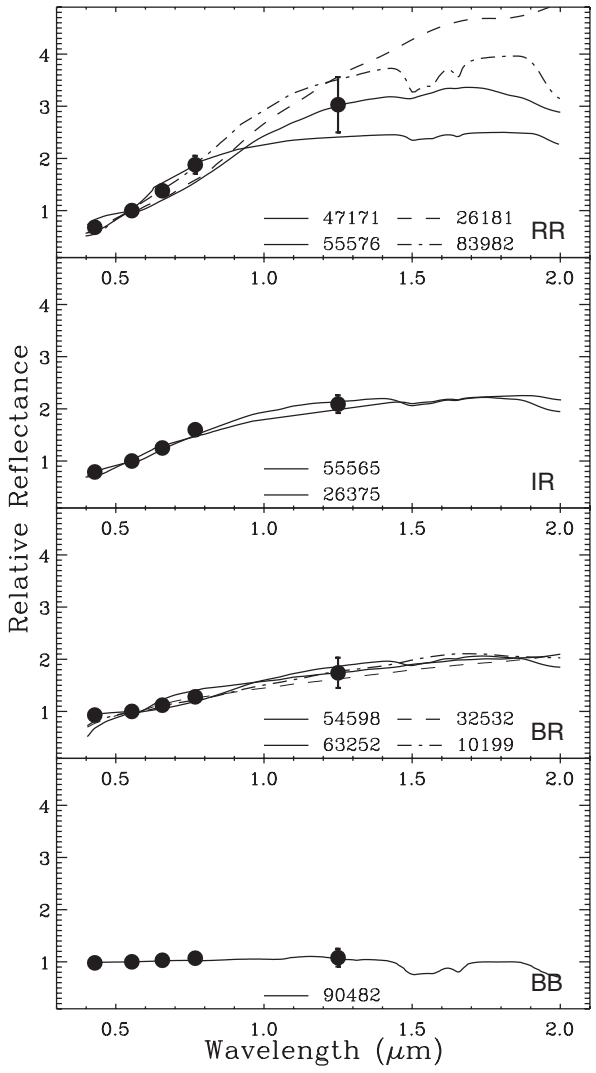

Fig. 1. Each of the four color classes is shown with the average broadband reflectance data (solid circles) and their relative error bars, normalized to the V band (0.55 μm). Overlain on each group is a compositional model of one or more well-observed members of the group. For RR the spectral models of (47171) 1999 TC_{36} (*Dotto et al.,* 2003a), (26181) 1996 GQ_{21} (*Doressoundiram et al.,* 2003), (55576) 2002 GB_{10}, and (83982) 2002 GO_9 (*Doressoundiram et al.,* 2005a,b) are shown; for BB the model of 90482 Orcus (*Fornasier et al.,* 2004a); for IR the models of (26375) 1999 DE_9 (*Doressoundiram et al.,* 2003) and (55565) 2002 AW_{197} (*Doressoundiram et al.,* 2005a,b); for BR the models of (63252) 2001 BL_{41} (*Doressoundiram et al.,* 2005a,b), 10199 Chariklo (*Dotto et al.,* 2003b), 54598 Bienor (*Dotto et al.,* 2003a), and 32532 Thereus (*Barucci et al.,* 2002).

properties and albedo. As noted above, only about 20 bright members of the TNO and Centaur populations have been well studied in both visible and near-infrared wavelengths and rigorously modeled. The spectra of TNOs and Centaurs have common behavior and their surface characteristics seem to show wide diversity. Several objects seem to show heterogeneity in their surfaces, such as 31824 Elatus (*Bauer et al.,* 2003a), 19308 1996 TO_{66} (*Brown et al.,* 1999), and 32532 Thereus (*Barucci et al.,* 2002; *Merlin et al.,* 2005). In some cases, observed surface variations may be attributed to different viewing geometry, and possibly the low signal precision of some of the observational data.

Several large and relatively bright objects have been discovered in the last few years, thus enabling spectroscopic observations with large groundbased telescopes. The spectral reflectance of 90482 Orcus can be matched with a model consisting of kerogen (a red-colored complex and relatively refractory organic solid), amorphous carbon, and H_2O ice (*Fornasier et al.,* 2004a; *de Bergh et al.,* 2005). *Jewitt and Luu* (2004) detected crystalline water on 50000 Quaoar; its presence may imply melting by resurfacing events, since the expected low temperature of formation suggests that amorphous ice should dominate. TNO 90377 Sedna resembles Triton (*Barucci et al.,* 2005b), while the largest presently known object of the TNOs population, 2003 UB_{313}, has a near-infrared spectrum very similar to that of Pluto (*Brown et al.,* 2005) (see below).

3.2. Groupings of Transneptunian Objects by Spectroscopic Characteristics

A sufficient number of TNOs have been observed spectroscopically in the region 0.3–2.5 μm to see categories into which they fall. We do not propose the following as a taxonomy, but note the basic characteristics of these groups.

1. Objects having absorption bands of H_2O ice that, when sufficiently well defined, reveal the crystalline rather than amorphous phase. These objects exhibit a range of redness and geometric albedo similar to the previous class.

2. Objects having absorption bands of solid CH_4 with a wide range of band strengths from weak to heavily saturated. Two subclasses are seen:

2a. Absorption bands of both CH_4 and N_2; in this situation the CH_4 is often dissolved in N_2 ice. Pluto and (probably) Sedna share these properties, together with Neptune's satellite Triton.

2b. Absorption bands of CH_4 in the absence of N_2, and a clear indication that the CH_4 ice is pure and not dissolved in another ice. Examples are 2003 UB_{313} and 2005 FY_9.

3. Objects having no spectral features (0.3–2.5 μm), but a wide range of colors, represented by degrees of positive spectral slope toward longer wavelengths (red color). Some objects are essentially neutral (gray) over this spectral interval, while others are among the reddest objects in the solar system. Geometric albedos appear to lie in the range 0.03–0.2.

3.3. 90377 Sedna and 2003 UB_{313}: Two Objects of Special Interest

The object 90377 Sedna belongs to the dynamical class called the extended scattered disk, with the most distant perihelion at 76 AU presently known. *Barucci et al.* (2005b) reported visible and near-infrared observations showing a similarity to the spectrum of Triton, in particular in terms of the presence of absorption bands of N_2 and CH_4 in the 2.0–2.5-μm range.

Cross-correlation investigation gives a high level of confidence that the spectrum of Sedna has the same spectral bands as that of Triton (*Cruikshank et al.,* 2000) in the 2.0–2.45-μm wavelength region. A model of the Sedna spectrum (Fig. 2) calculated using the radiative transfer theory developed by *Shkuratov et al.* (1999) reproduces the spectrum well with an intimate mixture of 24% Triton tholin, 7% amorphous carbon, 10% N_2 ice, 26% CH_3OH ice, and 33% CH_4 ice contaminated by small inclusions of Titan tholin. Its composition could imply that during its perihelion passage, Sedna may have a temporary and thin N_2 atmosphere.

Brown et al. (2005) discovered an object larger than Pluto in a highly inclined orbit in the scattered Kuiper belt; it is currently designated 2003 UB_{313}. While this object is nearly neutral in color in the extended visible wavelength region, its near-infrared spectrum shows a complex of methane ice absorptions very similar to Pluto (Fig. 3). The solid N_2 band at 2.15 μm that is visible in the spectra of Pluto and Triton cannot be reliably detected in the existing data. An analysis of the central wavelengths of the CH_4 bands does not show the shift in wavelength (the matrix shift) seen in the spectra of Pluto and Triton and attributed to the fact that most (Triton) or some (Pluto) of the CH_4 is dissolved in solid N_2. The CH_4 on 2003 UB_{313} is thus thought to be present largely in its pure form (*Brown et al.,* 2005).

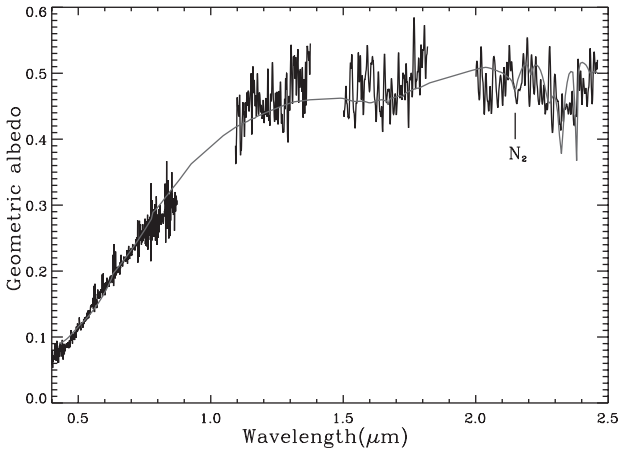

Fig. 2. The spectrum of 90377 Sedna, 0.4–2.5 μm. The best-fitting model is overlain as a continuous line. The geometric albedo is 0.15 at 0.55 μm (*Barucci et al.,* 2005b).

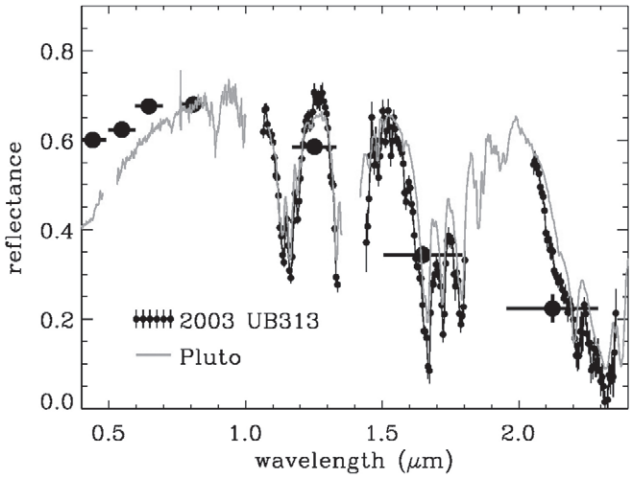

Fig. 3. Relative reflectance of 2003 UB_{313} (filled circles with error bars) and absolute reflectance of Pluto (gray line). The reflectance derived from BVRIJHK photometry is shown by the large points. The UB_{313} spectrum is scaled to match Pluto at 0.8 μm. From *Brown et al.* (2005), reproduced courtesy of *The Astrophysical Journal*.

4. THERMAL INFRARED SPECTROSCOPY

The Infrared Spectrograph (IRS) on the Spitzer Space Telescope brings thermal emission spectroscopy of the brightest Centaurs and KBOs within reach. The mid-infrared (5–38 μm) is well suited to investigating the silicate fraction of the surface layer of these objects because it contains the Si-O stretch and bend fundamental molecular vibration bands (typically 9–12 and 14–25 μm, respectively). Interplay between surface and volume scattering around these bands creates complex patterns of emissivity highs and lows that are very sensitive to, and therefore diagnostic of, mineralogy (e.g., *Salisbury et al.,* 1992; *Hapke,* 1996; *Cooper et al.,* 2002). We include Trojan asteroids in this section because they may be genetically related to Centaurs, they have similar emissivity spectra to at least one Centaur, and they are more accessible than the Centaurs and KBOs.

4.1. Trojan Asteroids

Trojan asteroids are located beyond the main belt, trapped in Jupiter's stable Lagrange points at 5.2 AU (leading and trailing the planet by 60° in its orbit). They typically have albedos of a few to several percent (e.g., *Cruikshank,* 1977; *Fernandez et al.,* 2003). Their reflectance spectra in the visible and near-infrared (0.3–4.0 μm) generally are featureless with moderately red spectral slopes, comparable to class BB and BR Centaurs and KBOs (e.g., *Jewitt and Luu,* 1990; *Luu et al.,* 1994; *Dumas et al.,* 1998; *Emery and Brown,* 2003; *Fornasier et al.,* 2004b) (see also section 2.1). Emissivity spectra of three Trojan asteroids have been measured with Spitzer: 624 Hektor, 911 Agamemnon, and 1172 Aneas (*Emery et al.,* 2006) (Fig. 4). The emissivity spectrum is defined as the measured flux spectrum divided by modeled thermal continuum.

The emissivity spectra of all three Trojans exhibit emission bands with strong spectral contrast after the underlying thermal continuum throughout the 5–38-μm region is removed (Fig. 4). *Emery et al.* (2006) interpret the strong emissivity plateau near 10 μm and the broader emissivity high near 20–25 μm to indicate the presence of fine-grained silicates (Fig. 5); large grains show emissivity lows at these wavelengths (e.g., *Christensen et al.,* 2000). In addition, the emissivity bands in Trojans also do not exactly match those expected for regolith surfaces; the 10-μm plateau is narrower and the spectra do not rise as rapidly near 15 μm. Surface structure and grain size may be playing an important role; a surface composed of silicate grains that are tens or hundreds of micrometers in size show a 10-μm absorption band, while grains smaller than about 10 μm (dispersed, as in a comet's coma) show the characteristic band in emission. On a solid surface, in the absence of a suspending medium, emission from fine-grained silicate particles imbedded in a matrix that is fairly transparent at these wavelengths (e.g., macromolecular organic solids) may explain the occurrence of the emissivity peak attributed to silicates (*Emery et al.,* 2006). Grain size and surface microstructure are relevant because they are indicators of the mechanisms of origin and evolution of the surfaces of airless bodies exposed to the local environment of collisional regolith gardening, and bombardment by micrometeoroids and atomic particles over the age of the solar system. Although we are only beginning to understand these processes in various regions of the solar system, their importance in deciphering surface evolution is generally recognized (e.g., *Clark et al.,* 2002).

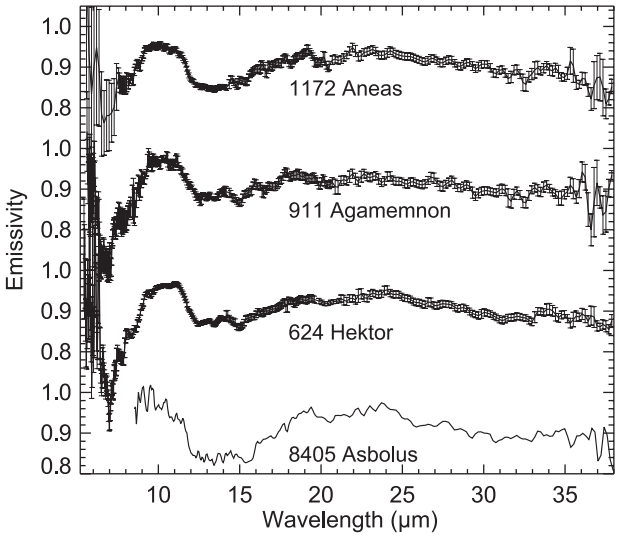

Fig. 4. Spectra of three Trojan asteroids measured with the Spitzer Space Telescope.

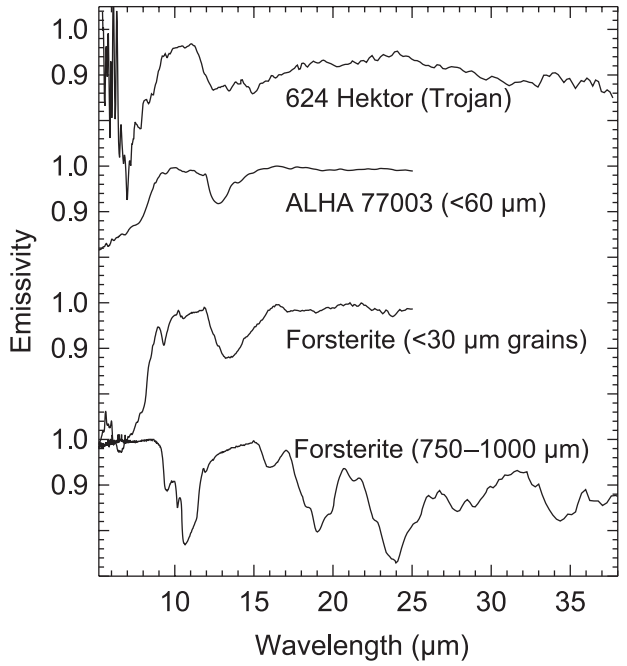

Fig. 5. The emissivity spectrum of Hektor is compared with laboratory spectra of a meteorite and minerals. The fine-grained forsterite (Fo_{88}) and the carbonaceous (CO3) meteorite ALHA 77003 are from the ASTER database (*speclib.jpl.nasa.gov*) (*Salisbury et al.,* 1992), and the large-grained forsterite is from the spectral library at Arizona State University (*tes.asu.edu/speclib*) (*Christensen et al.,* 2000).

4.2. Centaurs and Kuiper Belt Objects

Since these objects are at larger heliocentric distances than Trojans, they are cooler and thus observable only at the longer wavelengths of the IRS spectral range. An early program on Spitzer included two Centaurs that were observed from 7.5 to 38 μm, and four Centaurs in the range 14.2–38 μm. An additional 11 Centaurs and KBOs were observed only in the region 20–38 μm. The Centaur 8405 Asbolus was bright enough to be observed from 7.5 to 38 μm; in this region its spectrum is very similar to those of the Trojan asteroids.

Because the other Centaurs and KBOs are significantly fainter, the quality of the spectra is much lower. Longward of 20 μm, the spectrum of Pholus displays no diagnostic bands, despite having a feature-rich near-infrared reflectance spectrum (*Cruikshank et al.,* 1998).

5. MODELS OF PLANETARY SURFACES

5.1. General Remarks

Before describing the spectral models for each of the four taxa presented in section 2 and for the spectra of individual objects, it is useful to review the state of modeling of diffuse reflectance from the surfaces of airless bodies, and to note some of the directions this work is currently taking.

For the spectral region in which reflected sunlight dominates the observed flux from an airless body, quantitative models of diffuse reflectance require the computation of the full spectral reflectance properties, which include not only the spectral shape, but the absolute reflectance (characterized by geometric albedo) across the full range of wavelengths for which observations exist. In these calculations, the formulations of *Hapke* (1981, 1993) and *Shkuratov et al.* (1999) are often used. In addition to the original literature sources, the discussion of the practical application of Hapke theory to reflectance spectroscopy of solid surfaces by *Verbiscer and Helfenstein* (1998) is particularly useful (see also *McEwen,* 1991). *Poulet et al.* (2002) have compared the Hapke and Shkuratov theories in the context of modeling solid surfaces, and *Cruikshank et al.* (2004) have described the computational procedures in more general terms.

The naturally occurring materials on a planetary surface can be segregated from one another or can be mixed in various combinations in a number of ways that affect the scattering properties and the abundances derived from the synthetic spectra calculated from scattering theories to match the observed spectra. These mixing scenarios have been discussed in various publications, including those cited in the previous paragraph.

5.2. Materials that May Impart Red Color

While a modest degree of red color, such as that of Trojan asteroid 624 Hektor, can be explained by the presence of the mineral Mg-rich pyroxene (*Cruikshank et al.,* 2001; *Emery and Brown,* 2003), redder objects require other materials that are not minerals. *Gradie and Veverka* (1980) introduced the concept of *organic solids* to explain the red color of the D-type asteroids, suggesting the presence of " . . . very opaque, very red, polymer-type organic compounds, which are structurally similar to aromatic-type kerogen." They compared the reflectance spectra of the D-type asteroids to mixtures of montmorillonite (clay), magnetite (iron oxide), carbon black, and a coal-tar residue (kerogen) that was insoluble in organic solvents, and found a satisfactory match for both the low albedo and the red color of this specific class of asteroids. Organic kerogen-like structures consisting of small aromatic moieties connected by short aliphatic bridging units are found in carbonaceous meteorites (*Kerridge et al.,* 1987), and the presence of similar structures in interstellar dust grains has also been deduced from infrared spectra of dusty diffuse interstellar clouds (*Pendleton and Allamandola,* 2002).

Tholins, which are the refractory residues from the irradiation of gases and ices containing hydrocarbons, have color properties that make them reasonable candidates for comparison to the spectra of solar system bodies. A number of tholins have been prepared in the context of the photochemical aerosols in Titan's atmosphere (e.g., *Khare et al.,* 1984; *Coll et al.,* 1999; *Ramíriz et al.,* 2002; *Tran et al.,*

2003; *Imanaka et al.,* 2004), and while they are optically (spectrally) quite similar to Titan, they have until recently proven difficult to analyze and characterize fully from a chemical point of view. Recent work by *Tran et al.* (2003) and *Imanaka et al.* (2004), for example, has greatly improved the analysis and characterization of a class of tholins produced by photolysis and cold plasma irradiation of gaseous mixtures. Optically, the tholins are characterized by strong absorption in the ultraviolet and visible spectral regions giving them strong yellow, orange, and red colors, high reflectance at longer wavelengths, and (in some cases) absorption bands characteristic of aliphatic and aromatic hydrocarbons with varying amounts of substituted nitrogen (*Cruikshank et al.,* 2005a).

5.3. Color Classes Compared with Models

Groups BB and BR defined above have color spectra very similar to those of C-type and D-type asteroids. Going from neutral (BB group) to very red (RR group) spectra requires a higher content of organic materials to fit approximately the characteristic spectrum of the each group. Groups BB and BR in general, as discussed by *Cruikshank and Dalle Ore* (2003), do not require the presence of organic materials to reproduce their behavior, while IR and RR groups require large amounts of tholins on the surface to reproduce their strong colors [see *Roush and Cruikshank* (2004) and *Cruikshank et al.* (2005a) for additional discussion of tholins in the solar system]. Water ice seems to be present in some spectra of all the groups.

The RR group contains the reddest objects of the solar system. Some well-observed objects are members of this group, such as 5145 Pholus, 47171 (1999 TC_{36}), 55576 (2002 GB_{10}), 83982 (2002 GO_9), and 90377 Sedna. All these objects appear to contain at least few percent of H_2O ice on the surface, while 5145 Pholus has absorption bands of methanol ice (*Cruikshank et al.,* 1998) in addition to H_2O. No known material other than tholins can simultaneously reproduce their redness and low albedo.

The BB group contains objects having neutral reflectance spectra. Typical objects in the group are 2060 Chiron, 90482 Orcus, 19308 (1996 TO_{66}), and 15874 (1996 TL_{66}). The spectra are in general flat, sometime bluish in the NIR. The H_2O ice absorption bands seem generally stronger than in the other groups, although the spectrum of 1996 TL_{66} is completely flat and the Chiron spectrum shows H_2O ice only at some times (it exhibits episodic cometary activity). Large amounts of amorphous carbon must be common to the members of this group.

The IR group is less red than the RR group. Typical members of this class are 20000 Varuna, 38628 Huya, 47932 (2000 GN_{171}), 26375 (1999 DE_9), and 55565 (2002 AW_{197}). Three of these objects show hydrous silicates on the surface.

The BR group is an intermediate group between BB and IR with colors closer to those of the IR group. Typical members of this class are 8405 Asbolus, 10199 Chariklo, 54598 Bienor, and 32532 Thereus. A few percent of H_2O is present on the surface of these objects, except Asbolus, for which *Barucci et al.* (2000) and *Romon-Martin et al.* (2002) found no ice absorption features during the object's complete rotational cycle.

The robust multivariate statistical analysis of broadband colors provides a strong indication for differences in the surface characteristics of the TNOs and Centaurs, while the classification scheme clearly indicates groupings with different physicochemical surface properties.

5.4. Nature Versus Nurture: What Do the Colors and Spectra of Transneptunian Objects Tell Us?

The color diversity at visible wavelengths of Kuiper belt objects and Centaurs has been recognized for a decade (e.g., *Luu and Jewitt,* 1996; *Tegler and Romanishin,* 1998; *Jewitt,* 2002). Investigators have noted many possible correlations between colors and dynamical characteristics, fueling what has become the TNO version of the classic "nature vs. nurture" debate in biology: Do the diverse colors reflect diverse primordial compositions, or do they result from diverse and different degrees of surface processing? Compelling arguments have been made on both sides, suggesting that both factors may influence colors.

The most robust color pattern reported to date is the redder visual colors of classical KBOs, first described by *Tegler and Romanishin* (2000). Classical KBOs are those in low-inclination, low-eccentricity, nonresonant orbits. Although the numbers vary, depending on which color index is used, it is clear that the color statistics of this subpopulation are significantly different from those of other TNO dynamical classes (e.g., *Boehnhardt et al.,* 2003), despite considerable diversity of opinions about how (or indeed, if) classical objects differ dynamically from other nonresonant dynamical classes.

Another color pattern that has been widely confirmed is a tendency for lower inclination objects to have redder colors (e.g., *Trujillo and Brown,* 2002; *Stern,* 2002a; *Doressoundiram et al.,* 2002; *Boehnhardt et al.,* 2002). However, since classical objects generally have lower inclinations and redder colors, and scattered objects have more neutral average colors and higher inclinations, much, if not all, of this trend could be due to the presence of red classical objects dominating the low-inclination end of the sample, and/or similar contamination from the more gray scattered population at the high-inclination end of the sample (e.g., *Peixinho et al.,* 2004; chapter by Chiang et al.).

Many additional trends have been proposed, and some will probably be confirmed as more data accumulate, but we will concentrate on the one (or two) described above. Part of our reasoning for restricting the focus at present is the risk of observational biases. We have already noted possible contamination of samples resulting from different dynamical classification schemes. Biases may also enter from inefficiencies in discovering particular types of objects. *Trujillo and Brown* (2002) noted an apparent paucity of gray

objects with perihelion distances q > 40, but showed that a sampling bias was probably at work. *Peixinho et al.* (2004) explored the dependence of color trends with q on absolute magnitude, and found the trend only seemed to affect the fainter objects, those most likely to be afflicted by observational biases.

5.4.1. Environmental influences. Many environmental influences have been hypothesized. Radiolysis and photolysis are thought to progressively darken the surfaces of icy outer solar system materials over time, initially at blue wavelengths, leading to very red materials. As higher doses accumulate, red wavelengths darken and blue wavelengths may even brighten somewhat, culminating in spectrally neutral coatings (e.g., *Strazzulla et al.,* 1998, 2003; *Moroz et al.,* 2003, 2004). Irradiation of ices found in TNOs also produces distinct chemical changes that have been studied in the laboratory (e.g., *Moore et al.,* 2003; *Gerakines et al.,* 2004). Cratering by large impactors should excavate more pristine material from deep below the radiation-processed surface zone. *Luu and Jewitt* (1996) proposed a collisional resurfacing model in which continuous radiolytic reddening competes with sporadic impacts bringing grayer material to the surface. They were able to reproduce the observed color diversity, but the model predicted a strong size-dependence of color as well as significant color variations as objects rotate, neither of which has been observed (*Jewitt and Luu,* 2001).

Delsanti at al. (2004) folded cometary activity into the model, showing that activity could mask regional color variations on larger objects, which can reaccrete the bulk of the dust lofted during an active episode, and thus change colors in a globally uniform way. Since larger objects are generally the ones that are observed, this may offer a way around the absence of color variation with rotation. While some Centaurs are known to show continuous or episodic cometary activity (e.g., *Luu and Jewitt,* 1990; *Bauer et al.,* 2003b; *Choi and Weissman,* 2006), among the TNOs there are no reported cases of volatile activity in the current epoch.

Gil-Hutton (2002) and *Cooper et al.* (2003) applied a more realistic approach to radiolysis, noting that energetic particle fluxes vary considerably through the transneptunian region. Closer to the Sun, solar wind protons and solar UV photons drive increasingly rapid chemical processing, while further out, charged particles diffuse in from the heliosphere termination shock region, resulting in higher fluxes at large heliocentric distances as well. In high-flux regions, radiolysis could progress so rapidly that it makes surfaces gray, rather than red. Minimum radiolysis rates probably occur somewhere between 40 and 80 AU, where the classical KBOs reside. *Cooper et al.* (2003) also note the potential importance of high-velocity interstellar dust grains and sputtering processes, both of which erode surfaces, exposing much shallower materials than large impacts do. These shallow materials could be radiolytically reddened even before being exposed at the surface, offering a mechanism for maintaining red surfaces, at least in regions experiencing lower radiation doses, such as the classical belt.

Stern (2002a) recast the apparent trend of color with inclination among nonresonant objects in terms of mean random collision speed. Higher-inclination objects tend to suffer higher-speed collisions with cold disk objects, since they pass through the cold disk with higher velocities relative to the cold disk. This scenario favored a collisional influence on color, although the absence of convincing color trends with mean collision speed among the objects of any individual dynamical class argues against it. Also, *Thébault and Doressoundiram* (2003) have noted that collision frequencies should depend strongly on eccentricity, but compelling correlations between color and eccentricity have not been seen.

5.4.2. Compositional influences. The Kuiper belt may have experienced considerable dynamical churning since its objects accreted (e.g., chapter by Chiang et al.). The mixing that ensued frustrates efforts to search for the signature of compositional trends in the protosolar nebula in TNO colors, as was done so successfully in the main asteroid belt. However, compositionally distinct source regions may have existed, and could have resulted in compositionally distinct classes of TNOs.

Tegler and Romanishin (1998) presented perhaps the first evidence for a primordial compositional influence on TNO colors with their report of a bimodal color distribution. It has since emerged that the bimodal signature came from the Centaurs in their sample (*Peixinho et al.,* 2003; *Tegler and Romanishin,* 2003). Bimodal Centaur colors do not necessarily challenge collisional resurfacing scenarios, if there are two distinct dynamical sources feeding Centaurs into the region of the major planets. For instance, erosion of the inner edge of the classical belt and of the inner edge of the scattered disk could sample two distinct color distributions, both explainable by environmental factors.

Barucci et al. (2005a) have argued that even the non-Centaurs exhibit subtle clustering in their colors, rather than a continuum between the gray and red ends of the color distribution. These sorts of clusters are difficult to reconcile with collisional resurfacing scenarios, which generally predict continuous color distributions.

Comparing the *Barucci et al.* (2001) color classes with the dynamical classification scheme of Chiang et al. (this volume), we find several interesting patterns. First, classical objects almost all have RR-type colors, consistent with their well-known redder color distribution (e.g., *Tegler and Romanishin,* 2000). Second, Centaurs and resonant objects show remarkably similar G-mode color distributions, both groups being dominated by BR and RR colors. Third, scattered objects have much higher frequencies of BB objects than other dynamical classes, but otherwise look similar to the resonant and Centaur color distributions. Some caution is required here, since no effort was made to control for biases, which could play a significant role, since good color data are generally only available for brighter TNOs and discovery and recovery rates strongly favor intrinsically brighter objects, those that come closer to the Sun, and those having more "normal" types of orbits.

6. SIZES AND ALBEDOS OF TRANSNEPTUNIAN OBJECTS

The sizes of TNOs are of interest for several reasons: (1) Our estimates of the mass distribution in the outer solar nebula depend on the third power of TNO sizes. (2) Their size in relation to the sizes of Jupiter-family comets reveals something about both the size distribution of TNOs, from which these comets are derived (*Levison and Duncan,* 1997), and potentially about the mechanisms by which TNOs are perturbed onto cometary orbits. (3) Once the size of an object is known, its albedo is also known, providing an important constraint for interpreting colors and spectra (e.g., *Grundy and Stansberry,* 2004). Albedo diversity, to the extent that it is not correlated with color and spectral diversity, provides additional insight into the mechanisms underlying the remarkable spectral reflectance diversity of the TNO population.

The sizes of some outer solar system objects have been determined by a variety of methods. The sizes of Pluto and Charon have been measured via stellar occultation (e.g., *Elliot and Young,* 1992), and they have also been mapped using the Hubble Space Telescope (HST) (*Buie et al.,* 1997; *Young et al.,* 1999). Using HST, *Brown and Trujillo* (2004) resolved the TNO Quaoar, and placed an upper limit on the size of Sedna (*Brown et al.,* 2004). Recently, *Rabinowitz et al.* (2006) placed constraints on the size and albedo of 2003 EL_{61} based on its short rotation period (3.9 h), the mass determined from the orbit of a satellite, and an analysis of the stability of a rapidly rotating ellipsoid. *Grundy et al.* (2005) used the masses of binary TNO systems and an assumed range of mass densities to place plausible limits on their sizes and albedos.

Measurements of thermal emission can also be used to also constrain the sizes, and thereby albedos, of unresolved targets. *Tedesco et al.* (2002) used Infrared Astronomical Satellite (IRAS) thermal detections of asteroids to build a catalog of albedos and diameters. IRAS also detected thermal emission from the Centaur object Chiron and the Pluto-Charon system, and those data were used to determine albedos and sizes for those objects (*Sykes et al.,* 1987, 1991, 1999). Advances in the sensitivity of far-infrared and submillimeter observatories have recently allowed the detection of thermal emission from a small sample of TNOs, providing the first meaningful constraints on their sizes and albedos (e.g., *Jewitt et al.,* 2001; *Lellouch et al.,* 2002; *Altenhoff et al.,* 2004).

6.1. The Radiometric Method

The radiometric method for determining albedos and sizes typically utilizes measurements of both the visible and thermal-infrared brightness of an object. The visible brightness is proportional to the product of an object's visible geometric albedo, p_V, and cross-sectional area, πr^2, while the thermal brightness depends on the bolometric albedo, A (which determines the temperature), and the cross-sectional area. Given knowledge or an assumption for the phase integral, q ($A = qp_V$), measurements of the visible and thermal brightness can in principle be combined to solve directly for both the size of the object and its albedo.

In practice the thermal flux depends sensitively on the temperature distribution across the surface of the object: Warm regions near the subsolar point dominate the thermal emission, and their temperature depends on the thermal inertial of the surface and the rotation vector of the object as well as the albedo. Thermal inertia is a measure of the resistance of surface materials to a change in temperature; it is related to the thermal conductivity, heat capacity, and density. There are two commonly employed end-member models for the distribution of temperature: the slow-rotator, or standard thermal model (STM), and the fast-rotator, or isothermal latitude model (ILM) (see *Lebofsky and Spencer,* 1989). The STM is based on the assumption of a nonrotating (or equivalently, zero thermal inertia) spherical object, and the temperature distribution is specified by $T(\theta) = T_0 \cos^{1/4}\theta$, where $T_0 = [(1–A)S/(\eta\varepsilon\sigma)]^{1/4}$ is the subsolar point temperature. Here θ is the angular distance from the subsolar point, S is the solar constant at the distance of the object, ε the bolometric emissivity, and σ is the Stefan-Boltzmann constant. The beaming parameter, η, is an assignable factor that accounts for the nonuniform angular distribution of thermal emission (infrared beaming). The ILM incorporates the assumption that the object is illuminated at the equator and rotating very quickly (or equivalently, with infinite thermal inertia). The resulting temperature distribution is $T(\phi) = T_0 \cos^{1/4}\phi$, where in this case the subsolar point temperature is given by $T_0 = [(1–A)S/(\pi\eta\varepsilon\sigma)]^{1/4}$ (note the factor of π).

While more sophisticated extensions to the STM and ILM include the effects of surface roughness and thermal inertia (*Spencer,* 1990), as well as viewing geometry (*Harris,* 1998), their effects are semiquantitatively captured by the parameter η (e.g., *Spencer et al.,* 1989; *Stansberry et al.,* 2006). Furthermore, thermal measurements at multiple wavelengths near the blackbody peak directly give the color-temperature of the surface, in which case the systematic uncertainties between STM- and ILM-derived albedos and sizes (or those from thermophysical models) largely disappear (see Fig. 6). Here we only present results for objects that we have detected at both 24 and 70 μm with Spitzer. For all these reasons, we restrict our discussion of our Spitzer observations of the thermal emission from KBOs to albedos and diameters based on the STM.

6.2. Results of the Radiometric Method

Radiometric detections of TNOs have been made using the Infrared Space Observatory (ISO), the James Clerk Maxwell Telescope (JCMT) in Hawaii, the 30-m IRAM submillimeter telescope in Spain, and the Spitzer Space Telescope. *Thomas et al.* (2000) reported the first thermal detection of a TNO (excepting Pluto/Charon) based on ISO observations at a wavelength of 90 μm. *Altenhoff et al.*

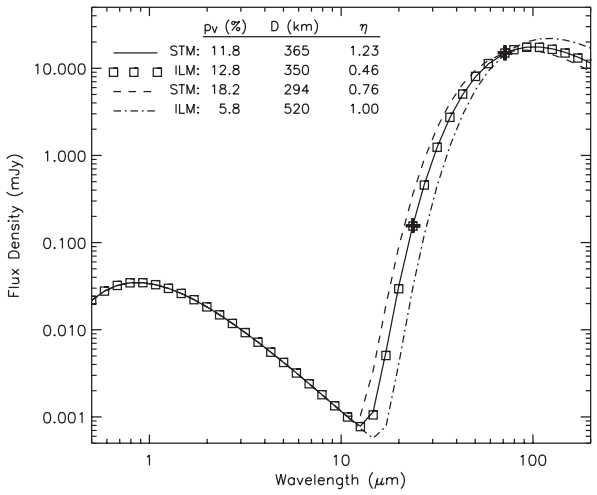

Fig. 6. Thermal models fitted to Spitzer data for (55565) 2002 AW_{197} (*Cruikshank et al.,* 2005b). All the models fit the visual magnitude. The heavy solid line and circles show the STM and ILM models fitted to both the 24 and 70 μm data, where η was allowed to be a free parameter. The resulting diameters and albedos are very similar. The dashed and dash-dot lines show STM and ILM models with the canonical values for η, and are fitted to just the 70-μm data point. The resulting diameters and albedos are highly discrepant, demonstrating the power of measuring thermal emission in two bands for determining albedos and sizes via the radiometric method.

(2004) report submillimeter measurements or limits for six TNOs, and review the observations of Varuna (*Jewitt et al.,* 2001; *Lellouch et al.,* 2002) and 2002 AW_{197} (*Margot et al.,* 2004). The IRAM submillimeter data were all taken at a wavelength of 1.2 mm. *Grundy et al.* (2005) also reanalyzed the submillimeter data from all four of those studies using a consistent thermal-modeling approach. *Cruikshank et al.* (2005b) and *Stansberry et al.* (2005, 2006) have reported Spitzer observations of six TNOs at wavelengths of 24 and 70 μm.

Table 2 summarizes the albedos and diameters of TNOs from all these studies, as well as providing values for the absolute magnitude and the spectral slope in the visible. In many cases *Grundy et al.* (2005) derived values from submillimeter observations that were in basic agreement with those found in the original studies. In these cases we have only included the original values. In a number of instances albedos and diameters are constrained by more than one measurement or method. In particular, a number of targets have been observed by both Spitzer and in the submillimeter. In general the submillimeter albedos are lower than those from Spitzer, and the submillimeter diameters correspondingly higher. While this discrepancy is not large, it may be systematic, and is significant at about the 2σ level (relative to flux uncertainties given in the studies) for individual objects. Another interesting case is 47171 (1999 TC_{36}). Both the Spitzer and submillimeter data indicate that it is considerably larger than was deduced by *Grundy et al.* (2005) by assuming a minimum plausible density of 0.5 g cm^{-3} and using the binary mass to deduce the size. *Stansberry et al.* (2006) derive a density of 0.5 (0.3–0.8) g cm^{-3} using their Spitzer size, with the density being about half as large using the size from *Altenhoff et al.* (2004).

Excluding objects with upper limits on their thermal fluxes and those with albedos ≥25%, the average geometric albedo of TNOs in Table 2 is 9 ± 5%, with the extremes being 2.5% (2001 QC_{298}) and 19% (28978 Ixion). Of the objects with albedos ≥25%, three are binaries [(47171) 1999 TC_{36}, (58534) 1997 CQ_{29}, and (66652) 1999 RZ_{253}] with albedos and sizes derived from assumed densities, and one is the Pluto-class object 2003 EL_{61}. If these binaries have densities <0.5 g cm^{-3} [the lower limit assumed by *Grundy et al.* (2005)], their albedos will be lower than shown in Table 2, and more in accord with the measured albedos. This may be a hint of the existence of many more TNOs of very low density. Object 2003 EL_{61}, with an albedo of 65%, could have high-albedo deposits of volatile ices by reason of its extreme size and very distant orbit. Its spectrum shows strong absorptions due to water ice (*Trujillo et al.,* 2005), and places fairly strong limits on the amount of CH_4 ice that could be present unless the grain size is miniscule. However, solid N_2 is very difficult to detect (particularly in the α-phase), and could easily produce the high albedo. It seems likely that its albedo is representative of a class of super-TNOs (Pluto/Charon, 2003 UB_{313}, Sedna, 2005 FY_9, 2003 EL_{61}) rather than of more typical TNOs.

6.3. Size and Albedo Determinations from Thermal Spectra

Just as direct radiometric observations yield information on the sizes and albedos of outer solar system bodies, spectra in the thermal region (described in section 4) can be similarly used. The emissivity spectra shown in section 4 were created by dividing the measured spectral energy distribution (SED) by a model of the thermal continuum. An estimate of the size and albedo of a body can be obtained by allowing the radius and albedo to vary in the model in order to find the best thermal continuum fit to the SED, just as was done with the Spitzer MIPS radiometry in section 5, but with a different dataset. The absolute calibration of IRS has an uncertainty of ~20%, which propagates to uncertainties of ~5% in the size estimate (see *Emery et al.,* 2006, for further discussion). The derived effective radii and albedos using the standard thermal model (STM) are listed in Table 3; close agreement with the MIPS radiometry is found in most cases.

7. MULTIPLICITY IN THE KUIPER BELT

The existence of numerous Kuiper belt binaries (hereafter abbreviated as KBB) has been revealed by a string of discoveries starting with the detection of the companion to 1998 WW_{31} in 2001 (*Veillet et al.,* 2002). Since then, the dis-

TABLE 2. Albedos and diameters of TNOs.

Object	H_v	S (%/100 nm)	Spitzer and ISO p_v (%)	Spitzer and ISO D (km)	Spitzer and ISO STM η	Submillimeter p_v (%)	Submillimeter D (km)	Ref.
(15789) 1993 SC		27.7	3.5 (2.2–5.1)	398 (227–508)				t
(15874) 1996 TL_{66}		0.74	>1.8	<958				t
(47171) 1999 TC_{36}	5.37	23.3	7.9 (5.8–11)	405 (350–470)*	1.2 (1.0–1.4)	5 (4–6)	609 (562–702)	s,a
(29981) 1999 TD_{10}	9.1	8.4	5.3 (3.8–7.8)	88 (73–104)	1.3 (1.0–1.6)			s
(55565) 2002 AW_{197}	3.62	16.5	12 (8.8–18)	734 (599–857	1.2 (1.0–1.4)	9 (7–11)	977 (890–1152)	s,m2
(28978) Ixion	4.04	16.8	19 (11–37)	480 (344–632)	0.6 (0.4–0.9)	>15	<804	s,a
(38628) Huya	5.1	17.7	6.6 (5.0–8.9)	500 (431–575	1 (0.9–1.2)	>8	<540	s,a
(20000) Varuna	3.94	17.9	14 (8.0–23)	586 (457–776)	1.6 (1.2–2.3)	6 (4–8)	1016 (915–1218)	s,j
(20000) Varuna						7 (4–10)	914 (810–1122)	l
			Other Approaches		Method			
(19308) 1996 TO_{66}	4.77	1.382	>3.8	<902	submillimeter limit			a,g
(19521) Chaos	4.95	18.958	>6.6	<748	submillimeter limit			a,g
(24835) 1995 SM_{55}	4.58	2.097	>7.6	<705	submillimeter limit			a,g
(26308) 1998 SM_{165}	6.38	20.961	17 (9.5–24)	238 (184–292)	binary			m4,g
(47171) 1999 TC_{36}	5.39	23.322	25 (14–35)	309 (239–379)	binary			m4,g
(50000) Quaoar	2.74	20.392	10 (6.9–13)	1260 (1070–1450)	imaging			b2
(55636) 2002 TX_{300}	3.47	–0.471	>22	<712	submillimeter limit			or,g
(58534) 1997 CQ_{29}	7.38	18.401	44 (25–63)	77 (60–95)	binary			m4,n,g
(66652) 1999 RZ_{253}	6.03	23.094	31 (18–44)	170 (131–208)	binary			n,g
(84522) 2002 TC_{302}	4.94	0	>5.1	<1211	submillimeter limit			a,g
(88611) 2001 QT_{297}	7.01	20.346	9.8 (5.6–14)	168 (130–206)	binary			os,g
(90377) Sedna	1.2	35.924	>18	<1800	imaging			b4
1998 WW_{31}	7.76	0.477	6.0 (3.4–8.6)	152 (117–186)	binary			v,g
2001 QC_{298}	7.69	4.249	2.5 (1.4–3.5)	244 (189–299)	binary			m4,g
2003 EL_{61}	–0.26	0.36	65 (60–73)	2050 (1960–2500)	shape, rotation			

*Implies a density of 500 (300–800) kg m^{-3} (*Stansberry et al.,* 2006).

References: [a] *Altenhoff et al.* (2004); [b2] *Brown and Trujillo* (2004); [b4] *Brown and Trujillo* (2004); [g] *Grundy et al.* (2005); [j] *Jewitt et al.* (2001); [l] *Lellouch et al.* (2002); [m2] *Margot et al.* (2002); [m4] *Margot et al.* (2004); [n] *Noll et al.* (2004b); [os] *Osip et al.* (2003); [or] *Ortiz et al.* (2004); [v] *Veillet et al.* (2002).

TABLE 3. Best fit parameters for the standard thermal model (STM).

Object	H_v*	R (km)	p_v	η	T_{ss} (K)
Hektor	7.49	110.0	0.038	0.95	179.4
Agamemnon	7.89	71.5	0.062	0.89	175.3
Aneas	8.33	69.1	0.044	0.96	170.4
Pholus	7.65	74.2	0.072	1.42	85.4
Asbolus	8.96	50.7	0.046	0.91	148.3
1999 RG_{33}	12.10	8.1	0.100	0.42	143.3
1999 TD_{10}	8.64	49.4	0.065	1.48	97.0
Elatus	10.98	17.9	0.057	0.89	125.0

*H_v is from the IAU Minor Planet Center. We assume G = 0.15 for all objects except Pholus and Elatus, for which G = 0.16 and 0.13, respectively, have been derived.

coveries have accumulated rapidly so that now a total of 25 KBBs are known in 22 systems (Table 4).

Gravitationally bound systems are important in three ways. First, they are tools for measuring the masses of Kuiper belt objects by observing their mutual orbits. Second, the frequency of binaries in separate dynamical populations may provide important clues on the origin and survival of these bound systems. Third, they are an important detail in understanding the general nature of debris disks.

7.1. Orbital Properties of Kuiper Belt Binaries

Of the 22 known systems, orbits have been observed for a subset of nine. For each of these nine systems, observation of the relative separation of the components and their orientation at a number of different epochs forms the basis for determining the binary orbit. The steps involved in orbit determination, while conceptually simple, are often difficult in practice because of the observational challenges and consequent sparseness of most datasets. The large range of uncertainties shown in Table 4 reflects these observational challenges.

As with many other measurable quantities in the Kuiper belt, the binary orbits show a large diversity in semimajor axis, eccentricity, and period. The shortest period so far determined is for the Pluto/Charon system at 6.4 d while the longest period (2001 QT_{297}) is roughly 100× greater. The most widely separated system, 2001 QW_{322}, had components separated by ~4 arcsec at the time of discovery (*Kavelaars et al.,* 2001). The lower limit is set by observational limitations with the closest reported binary separation being the 15 milliarcsec (0.2 pixel) separation of 1995 TL_8, an unresolved pair identified through PSF-fitting of data obtained with HST (*Stephens and Noll,* 2006). Theoretical studies (*Goldreich et al.,* 2002) do not indicate any reason

TABLE 4. Binary Kuiper belt objects.

Object	Class*	a (km)†	e†	P (d)†	M System (Zg)†	Ref.
Pluto (Charon)	3:2	19,636(8)	0.0076(5)	6.38722(2)	14,600(100)	[1]
(P1)						[2],[3]
(P2)						[2].[3]
(26308) 1998 SM_{165}	2:1	11,310(110)		130(1)	6.8(2)	[4],[5]
(47171) 1999 TC_{36}	3:2	7,640(460)		50.4(5)	14(3)	[4],[5]
2003 EL_{61}	S	49,500(400)	0.050(3)	49.12(3)	4,200(100) [7]	[6]
2001 QC_{298}	S	3,690(70)		19.2(2)	10.8(7)	[4],[5]
(82075) 2000 YW_{134}	S					[8]
(48639) 1995 TL_{8}	S					[8]
2003 UB_{313}	S					[7]
(88611) 2001 QT_{297}	C	31,409(2500)	0.31(8)	876(227)	3.2(3/2)	[9],[10]
1998 WW_{31}	C	22,300(800)	0.82(5)	574(10)	2.7	[11]
(58534) 1997 CQ_{29}	C	8,010(80)	0.45(3)	312(3)	0.42(2)	[12]
(66652) 1999 RZ_{253}	C	4,660(170)	0.460(13)	46.263(6/74)	3.7(4)	[13]
2001 QW_{322}	C					[14]
2000 CF_{105}	C					[15]
2000 CQ_{114}	C					[16]
2003 UN_{284}	C					[17]
2003 QY_{90}	C					[18]
2005 EO_{304}	C					[19]
(80806) 2000 CM_{105}	C					[8]
2000 OJ_{67}	C					[8]
(79360) 1997 CS_{29}	C					[8]
1999 OJ_{4}	C					[8]

*Dynamical classes: S = scattered disk, C = cold classical, n:m = resonant.
†Uncertainty in last significant digit(s) indicated in parentheses.

References: [1] *Tholen and Buie* (1997); [2] *Weaver et al.* (2006); [3] *Buie et al.* (2006); [4] *Margot et al.* (2004); [5] Grundy and Noll (personal communication, 2004); [6] *Brown et al.* (2005); [7] *Brown et al.* (2006); [8] *Stephens and Noll* (2006); [9] *Osip et al.* (2003); [10] *Kern* (2005); [11] *Veillet et al.* (2002); [12] *Noll et al.* (2004a); [13] *Noll et al.* (2004b); [14] *Kavelaars et al.* (2001); [15] *Noll et al.* (2002); [16] *Stephens et al.* (2004); [17] *Millis and Clancy* (2003); [18] *Elliot et al.* (2003); [19] *Kern and Elliot* (2005).

to suspect a lower limit to binary separation, and the large-amplitude, long-period lightcurve of 2001 QG_{298} suggests it as a candidate member of a potentially significant population (~10–20%) of near-contact binaries (*Sheppard and Jewitt,* 2004).

So far, none of the nine measured systems have orbits that are known well enough that the timing of mutual transits and occultations can be predicted with certainty. Because the KBB components typically have diameters of hundreds of kilometers, mutual event observability is strongly biased toward systems with shorter periods (smaller semimajor axes). These are among the most recently discovered and least well characterized in terms of orbits. Several ongoing observational programs are measuring the orbits of additional KBBs, so the list is likely to expand and uncertainties are likely to decrease on relatively short timescales.

7.2. Physical Properties of Kuiper Belt Binaries and Multiples

The determination of mutual orbital period and semimajor axis allows the measurement of the total system mass following Kepler's second law. For six of the nine systems the mass is determined to an uncertainty of 10% or better. Masses range from a low of 0.42 Zg (1 Zg = 10^{18} kg) for (58534) 1997 CQ_{29} to 14,600 Zg for Pluto.

Even in the absence of size information, the availability of mass information makes it possible to constrain two other physical parameters of interest, albedo and density. If photometric data at optical or near-infrared wavelengths are available (i.e., the reflected sunlight portion of the spectrum) it is possible to constrain albedo and density to lie along a well-defined function with albedo varying as the 2/3 power of the density. This derived information can be usefully reported as the geometric albedo in a given wavelength band at a reference density; a typical choice is to report the Cousins R band geometric albedo for an assumed density of 1000 kg/m^3. Derived albedos using this method show a very broad range (*Noll et al.,* 2004a,b; J.-L. Margot, personal communication), suggesting significant differences among the surfaces of KBBs. No strong trends of albedo of KBOs with other measurable quantities appear in the current set of available data, which includes both binaries and singles with measured albedos (*Grundy et al.,* 2005). The calculation of geometric albedo is subject to an uncertain phase correction. Most authors have used $\beta = 0.15$ mag/degree ($G = -0.21$) found by *Sheppard and Jewitt* (2002). The binary 1997 CQ_{29} has a surprisingly high albedo of $p_R = 0.37$

($\rho = 1000$ kg/m^3)$^{2/3}$ for a primary that would be only ~40 km in diameter (*Noll et al.,* 2004a).

When the diameter of at least one component of a binary is known, either from direct measurements or indirectly from thermal emission observations and modeling, it is possible to uniquely constrain the density of the object. This is useful for removing the density dependence of albedo, as discussed above. Even more importantly, the density provides constraints on the internal structure of an object including constraints on mixtures of cosmogonically plausible compositions and internal macro- and microporosity. Beyond the Pluto-Charon binary (*Buie et al.,* 2006), this information is currently published for only two objects, (47171) 1999 TC_{36} (*Stansberry et al.,* 2005) and 2003 EL_{61} (*Brown et al.,* 2005). *Stansberry et al.* (2005) find a density of 550–800 kg/m^3 for (47171) 1999 TC_{36}. The extremely low density requires a very high porosity for plausible compositions and at the lowest densities, highest porosities raises the question of whether it can be consistent with compaction expected in a self-supported sphere of diameter ~325–425 km. One possible explanation suggested by Stansberry et al. is that the primary of (47171) 1999 TC_{36} is itself a close binary. By decreasing the enclosed volume for a given surface area, the apparently anomalously low density is partly mitigated.

7.3. Formation and Destruction of Kuiper Belt Binaries

Objects in the Kuiper belt are grouped by their heliocentric orbital properties into dynamical families. Binaries detectable with current data appear to be significantly more common in the so-called cold classical Kuiper belt than in other populations (*Stephens and Noll,* 2006). The reason for the prevalence of binaries among the dynamically cold objects in the Kuiper belt may be related to formation mechanisms and/or to subsequent events that may have destroyed preexisting binaries.

None of the formation models proposed to date can form binaries in the current Kuiper belt (*Stern,* 2002b; *Weidenschilling,* 2002; *Goldreich et al.,* 2002; *Funato et al.,* 2004; *Astakhov et al.,* 2005); all require a 100-fold or more higher density of objects. This points to a primordial origin for KBBs and is consistent with models of early solar system evolution that predict 2 or more orders of magnitude reduction in the surface mass density in the Kuiper belt from the orbital migration of Neptune (*Levison and Morbidelli,* 2003). The observed prevalence of binary systems with similar-mass components (i.e., m_2/m_1 on the order of 1) suggests chaos-assisted capture as the most likely mode of formation for most of the known KBBs (*Astakhov et al.,* 2005). Models of KBB survival predict the loss of roughly 10× the current number of widely separated KBBs, although most of the smaller-separation binaries can survive for 4.5 G.y. (*Petit and Mousis,* 2004).

Two multiple systems are now known in the transneptunian region. The satellites in these systems have small masses relative to their primaries, which together with their orbital properties and the large masses of the primaries suggests a mode of formation other than capture. Preliminary orbits determined for the two newly discovered satellites of Pluto are consistent with zero or low eccentricity (P2 and P1 respectively) (*Weaver et al.,* 2006; *Buie et al.,* 2006), suggestive of formation in a post-giant-impact accretion disk (*Stern et al.,* 2006) that would also be consistent with the proposed impact origin for Charon (*Canup,* 2005). Object 2003 EL_{61} has two reported satellites (*Brown et al.,* 2005, 2006) and the authors speculate that these may also be compatible with an impact origin. It appears that, as is the case with other physical properties of KBOs, bound systems in the Kuiper belt come in a fascinatingly diverse variety, begging for further study.

8. SUMMARY AND CONCLUSIONS

TNOs are remnants of the protoplanetary disk in which the accretion of the planetesimals that built the giant planets occurred. TNO population statistics and dynamics demonstrate that the region beyond Neptune has not been stable since the planets formed, having been dynamically disrupted by the outward migration of Uranus and Neptune, with the possibility of significant mass loss resulting from mutual collisions.

In this chapter we have shown that the physical properties of TNOs are highly varied in every respect: size, color, reflectance (albedo), surface composition, mean density, and multiplicity. The diversity in all these parameters suggests that the TNOs represent a substantial range in original bulk composition, with differing fractions of ices, silicates, and organic solids; all these components are found in interstellar dust in giant molecular clouds. An alternative view suggests that varying degrees of postaccretional processing of bodies of approximately uniform composition have produced the colorful tableau of physical properties that has emerged from just over a decade of physical studies of these objects.

REFERENCES

Altenhoff W. J., Bertoldi F., and Menten K. M. (2004) *Astron. Astrophys., 415,* 771–775.

Astakhov S. A., Lee E. A., and Farrelly D. (2005) *Mon. Not. R. Astron. Soc., 360,* 401–415.

Barucci M. A., Capria M. T., Coradini A., and Fulchignoni M. (1987) *Icarus, 72,* 304–324.

Barucci M. A., de Bergh C., Cuby J.-G., Le Bras A., Schmitt B., and Romon J. (2000) *Astron. Astrophys., 357,* L53–L56.

Barucci M. A., Fulchignoni M., Birlan M., Doressoundiram A., Romon J., and Boehnhardt H. (2001) *Astron. Astrophys., 371,* 1150–1154.

Barucci M. A., Boehnhardt H., Dotto E., Doressoundiram A., Romon J., et al. (2002) *Astron. Astrophys., 392,* 335–339.

Barucci M. A., Belskaya I. N., Fulchignoni M., and Birlan M. (2005a) *Astron. J., 130,* 1291–1298.

Barucci M. A., Cruikshank D. P., Dotto E., Merlin F., Poulet F., et al. (2005b) *Astron. Astrophys., 439,* L1–L4.

Bauer J. M., Meech K. J., Fernández Y. R., Pittichova J., Hainaut O. R., Boehnhardt H., and Delsanti A. C. (2003a) *Icarus, 166,* 195–211.

Bauer J. M., Fernandez Y. R., and Meech K. J. (2003b) *Publ. Astron. Soc. Pac., 115,* 981–989.

Boehnhardt H., Delsanti A., Barucci A., Hainaut O., Doressoundiram A., et al. (2002) *Astron. Astrophys., 395,* 297–303.

Boehnhardt H., Barucci M. A., Delsanti A., De Bergh C., Doressoundiram A., et al. (2003) *Earth Moon Planets, 92,* 145–156.
Brown M. E. and Trujillo C. A. (2004) *Astron. J., 127,* 2413–2417.
Brown M. E., Trujillo C. A., and Rabinowitz D. (2004) *Astrophys. J., 617,* 645–649.
Brown M. E., Trujillo C. A., and Rabinowitz D. L. (2005) *Astrophys. J., 635,* L97–L100.
Brown M. E., van Dam M. A., Bouchez A. H., Le Mignant D., Campbell R. D., et al. (2006) *Astrophys. J., 639,* L43–L46.
Brown R. H., Cruikshank D. P, and Pendleton Y. (1999) *Astrophys. J., 519,* L101–L104.
Buie M. W., Tholen D. J., and Wasserman L. H. (1997) *Icarus, 125,* 233–244.
Buie M. W., Grundy W. M., Young E. F., Young L. A., and Stern S. A. (2006) *Astron. J., 132,* 290–298.
Canup R. M. (2005) *Science, 307,* 546–550.
Choi Y. J. and Weissman P. R. (2006) *IAU Circ. 8656*.
Christensen P. R., Bandfield J. L., Hamilton V. E., Howard D. A., Lane M. D., Piatek J. L., Ruff S. W., and Stefanov W. L. (2000) *J. Geophys. Res*., *105(E4),* 9735–9739.
Clark B. E., Hapke B., Pieters C., and Britt D. (2002) In *Asteroids III* (W. F. Bottke Jr. et al., eds.), pp. 585–599. Univ. of Arizona, Tucson.
Coll P., Coscia D., Smith N., Gazeau M.-C., Ramírez S. I., et al. (1999) *Planet Space Sci., 47,* 1331–1340.
Cooper B. L., Salisbury J. W., Killen R. M., and Potter A. E. (2002) *J. Geophys. Res., 107(E4),* 1–12.
Cooper J. F., Christian E. R., Richardson J. D., and Wang C. (2003) *Earth Moon Planets, 92,* 261–277.
Cruikshank D. P. (1977) *Icarus, 30,* 224–230.
Cruikshank D. P. and Dalle Ore C. M. (2003) *Earth Moon Planets, 92,* 315–330.
Cruikshank D. P., Roush T. L., Owen T. C., Geballe T. R., de Bergh C., et al. (1993) *Science, 261,* 742–745.
Cruikshank D. P., Roush T. L., Bartholomew M. J., Geballe T. R., Pendleton Y. J., et al. (1998) *Icarus, 135,* 389–407.
Cruikshank D. P., Schmitt B., Roush T. L., Owen T. C., Quirico E., et al. (2000) *Icarus, 147,* 309–316.
Cruikshank D. P., Dalle Ore C. M., Roush T. L., Geballe T. R., Owen T. C., et al. (2001) *Icarus, 153,* 348–360.
Cruikshank D. P., Roush T. L., and Poulet F. (2004) *C. R. Physique, 4,* 783–789.
Cruikshank D. P., Imanaka H., and Dalle Ore C. M. (2005a) *Adv. Space Res., 36,* 178–183.
Cruikshank D. P., Stansberry J. A., Emery J. P., Fernández Y. R., Werner M. W., Trilling D. E., and Rieke G. H. (2005b) *Astrophys. J., 624,* L53–L56.
de Bergh C., Boehnhardt H., Barucci M. A., Lazzarin M., Fornasier S., et al. (2004) *Astron. Astrophys., 416,* 791–798.
de Bergh C., Delsanti A., Tozzi G. P., Dotto E., Doressoundiram A., and Barucci M. A. (2005) *Astron. Astrophys., 437,* 1115–1120.
Delsanti A., Hainaut O., Jourdeuil E., Meech K. J., Boehnhardt H., and Barrera L. (2004) *Astron. Astrophys., 417,* 1145–1158.
Doressoundiram A., Peixinho N., de Bergh C., Fornasier S., Thébault P., Barucci M. A., and Veillet C. (2002) *Astron. J., 124,* 2279–2296.
Doressoundiram A., Tozzi G. P., Barucci M. A., Boehnhardt H., Fornasier S., and Romon J. (2003) *Astron. J., 125,* 2721–2727.
Doressoundiram A., Barucci M. A., Boehnhardt H., Tozzi G. P., Poulet F., de Bergh C., and Peixinho N. (2005a) *Planet. Space Sci., 53,* 1501–1509.
Doressoundiram A., Peixinho N., Doucet C., Mousis O., Barucci M. A., Petit J. M., and Veillet C. (2005b) *Icarus, 174,* 90–104.
Dotto E., Barucci M. A., Boehnhardt H., Romon J., Doressoundiram A., Peixinho N., de Bergh C., and Lazzarin M. (2003a) *Icarus, 164,* 408–414.
Dotto E., Barucci M. A., Leyrat C., Romon J., de Bergh C., and Licandro J.-M. (2003b) *Icarus, 164,* 122–126.
Douté S., Schmitt B., Quirico E., Owen T. C., Cruikshank D. P., et al. (1999) *Icarus, 142,* 421–444.
Dumas C., Owen T. C., and Barucci M. A. (1998) *Icarus, 133,* 221–232.
Elliot J. L. and Young L. A. (1992) *Icarus, 103,* 991–1015.
Elliot J. L., Kern S. D., and Clancy K. B. (2003) *IAU Circ. 8235.*
Emery J. P. and Brown R. H. (2003) *Icarus, 164,* 104–121.
Emery J. P., Cruikshank D. P., and Van Cleve J. (2006) *Icarus, 182,* 496–512.
Fernández Y. R., Sheppard S. S., and Jewitt D. C. (2003) *Astron. J., 126,* 1563–1574.
Fornasier S., Dotto E., Barucci M. A., and Barbieri C. (2004a) *Astron. Astrophys., 422,* L43–L46.
Fornasier S., Dotto E., Marzari F., Barucci M. A., Boehnhardt H., Hainaut O., and de Bergh C. (2004b) *Icarus, 172,* 221–232.
Fulchignoni M., Birlan M., and Barucci M. A. (2000) *Icarus, 146,* 204–212.
Funato Y., Makino J., Hut P., Kokubo E., and Kinoshita D. (2004) *Nature, 427,* 518–520.
Gerakines P. A., Moore M. H., and Hudson R. L. (2004) *Icarus, 170,* 202–213.
Gil-Hutton R. (2002) *Planet. Space Sci., 50,* 57–62.
Goldreich P., Lithwick Y., and Sari R. (2002) *Nature, 420,* 643–646.
Gradie J. and Veverka J. (1980) *Nature, 283,* 840–842.
Grundy W. M. and Stansberry J. A. (2004) *Earth Moon Planets, 92,* 331–336.
Grundy W. M., Noll K. S., and Stephens D. C. (2005) *Icarus, 176,* 184–191.
Hapke B. (1981) *J. Geophys. Res., 96,* 3039–3054.
Hapke B. (1993) *Theory of Reflectance and Emittance Spectroscopy.* Cambridge Univ., New York. 455 pp.
Hapke B. (1996) *J. Geophys. Res., 101,* 16833–16840.
Harris A. W. (1998) *Icarus, 131,* 291–301.
Imanaka H., Khare B. N., Elsila J. E., Bakes E. L. O., McKay C. P., et al. (2004) *Icarus, 168,* 344–366.
Jewitt D. C. (2002) *Astron. J., 123,* 1039–1049.
Jewitt D. C. and Luu J. X. (1990) *Astron. J., 100,* 933–944.
Jewitt D. C. and Luu J. X. (1993) *Nature, 362,* 730–732.
Jewitt D. C. and Luu J. X. (2001) *Astron. J., 122,* 2099–2114.
Jewitt D. C. and Luu J. X. (2004) *Nature, 432,* 731–733.
Jewitt D. C., Aussel H., and Evans A. (2001) *Nature, 411,* 446–447.
Kavelaars J. J., Petit J.-M., Gladman B., and Holman M. (2001) *IAU Circ*. *7749*.
Keller H. U., Britt D., Buratti B. J., and Thomas N. (2004) In *Comets II* (M. C. Festou et al., eds.), pp. 211–222. Univ. of Arizona, Tucson.
Kern S. D. (2005) Ph.D. thesis, Massachusetts Institute of Technology.
Kern S. D. and Elliot J. L. (2005) *IAU Circ. 8526*.
Kerridge J., Chang S., and Shipp R. (1987) *Geochim. Cosmochim. Acta, 51,* 2527–2540.
Khare B. N., Sagan C., Arakawa E. T., Suits R., Callcot T. A., and Williams M. W. (1984) *Icarus, 60,* 127–137.
Lazzarin M., Barucci M. A., Boehnhardt H., Tozzi G. P., de Bergh C., and Dotto E. (2003) *Astrophys. J., 125,* 1554–1558.
Lebofsky L. A. and Spencer J. R. (1989) In *Asteroids II* (R. P. Binzel et al., eds.), pp. 128–147. Univ. of Arizona, Tucson.
Lellouch E., Moreno R., Ortiz J. L., Paubert G., Doressoundiram A., and Peixinho N. (2002) *Astron. Astrophys., 391,* 1133–1139.
Levison H. F. and Duncan M. J (1997) *Icarus, 127,* 13–32.
Levison H. F. and Morbidelli A. (2003) *Nature, 426,* 419–421.
Luu J. and Jewitt D. (1990) *Astron. J., 100,* 913–932.
Luu J. and Jewitt D. (1996) *Astron. J., 112,* 2310–2318.
Luu J. X., Jewitt D. C., and Cloutis E. (1994) *Icarus, 109,* 133–144.
Margot J. L., Trujillo C., Brown M. E., and Bertoldi F. (2002) *Bull. Am. Astron. Soc., 34,* 871 (abstract).
Margot J. L., Brown M. E., Trujillo C. A., and Sari R. (2004) *Bull. Amer. Astron. Soc., 36*, 1081 (abstract).
McEwen A. S. (1991) *Icarus, 92,* 298–311.
McKinnon W. B, Lunine J. I., and Banfield D. (1995) In *Neptune and Triton* (D. P. Cruikshank, ed.), pp. 807–877. Univ. of Arizona, Tucson.
Merlin F., Barucci M. A., Dotto E., de Bergh C., and Lo Curto G. (2005) *Astron. Astrophys., 444,* 977–982.

Millis R. L. and Clancy K. B. (2003) *IAU Circ. 8251*.
Moore M. H., Hudson, R. L., and Ferrante R. F (2003) *Earth Moon Planets, 92,* 291–306.
Moroz L. V., Baratta G., Distefano E., Strazzulla G., Starukhina L. V., Dotto E., and Barucci M. A. (2003) *Earth Moon Planets, 92,* 279–289.
Moroz L. V., Baratta G., Strazzulla G., Starukhina L., Dotto E., Barucci M. A., Arnold G., and Distefano E. (2004) *Icarus, 170,* 214–228.
Noll K., Stephens D., Grundy W., Spencer J., Millis R., et al. (2002) *IAU Circ. 7857*.
Noll K. S., Stephens D. C., Grundy W. M., Osip D. J., and Griffin I. (2004a) *Astron. J., 128,* 2547–2552.
Noll K. S., Stephens D. C., Grundy W. M., and Griffin I. (2004b) *Icarus, 172,* 402–407.
Ortiz J. L., Sota A., Moreno R., Lellouch E., Biver N., et al. (2004) *Astron. Astrophys., 420,* 383–388.
Osip D. J., Kern S. D., and Elliot J. L. (2003) *Earth Moon Planets, 92,* 409–421.
Owen T. C., Cruikshank D. P., Roush T., DeBergh C., Brown R. H., et al. (1993) *Science, 261,* 745–748.
Peixinho N., Doressoundiram A., Delsanti A., Boehnhardt H., Barucci M. A., and Belskaya I. (2003) *Astron. Astrophys., 410,* L29–L32.
Peixinho N., Boehnhardt H., Belskaya I., Doressoundiram A., Barucci M. A., and Delsanti A. (2004) *Icarus, 170,* 153–166.
Pendleton Y. J. and Allamandola L. J. (2002) *Astrophys. J. Suppl., 128,* 75–98.
Petit J.-M. and Mousis O. (2004) *Icarus, 168,* 409–419.
Poulet F., Cuzzi J. N., Cruikshank D. P., Roush T., and Dalle Ore C. M. (2002) *Icarus, 160,* 313–324.
Quirico E., Douté S., Schmitt B., de Bergh C., Cruikshank D. P., et al. (1999) *Icarus, 139,* 159–178.
Rabinowitz D. L., Barkume K., Brown M. E., Roe H., Schwartz M., Tourtellotte S., and Trujillo C. (2006) *Astrophys. J., 639,* 1238–1251.
Ramírez S. I., Coll P., da Silva A., Navarro-González R., Lafait J., and Raulin F. (2002) *Icarus, 156,* 515–529.
Rietmeijer F. J. M., Nuth J. A. III, and Nelson R. N. (2004) *Meteoritics & Planet. Sci., 39,* 723–746.
Romon-Martin J., Barucci M. A., de Bergh C., Doressoundiram A., Peixinho N., and Poulet F. (2002) *Icarus, 160,* 59–65.
Roush T. L. and Cruikshank D. (2004) In *Astrobiology: Future Prospectives* (P. Ehrenfreund, ed.), pp. 149–177. Kluwer, Dordrecht.
Salisbury J. W., Walter L. S., Vergo N., and D'Aria D. M. (1992) *Mid-Infrared (2.1–25 μm) Spectra of Minerals*. Johns Hopkins Univ., Baltimore. 346 pp.
Sheppard S. S. and Jewitt D. C. (2002) *Astron. J., 124,* 1757–1775.
Sheppard S. S. and Jewitt D. (2004) *Astron. J., 127,* 3023–3033.
Shkuratov Y., Starukhina L., Hoffmann H., and Arnold G. (1999) *Icarus, 137,* 235–246.
Spencer J. R. (1990) *Icarus, 83,* 27–38.
Spencer J. R., Lebofsky L. A., and Sykes M. V. (1989) *Icarus, 78,* 337–354.
Stansberry J. A., Cruikshank D. P., Grundy W. G., Margot J. L., Emery J. P., Fernández Y. R., and Rieke G. H. (2005) *Bull. Am. Astron. Soc., 37,* 737 (abstract).
Stansberry J. A., Grundy W. M., Margot J. .L., Cruikshank D. P., Emery J. P., Rieke G. H., and Trilling D. E. (2006) *Astrophys. J., 643,* 556–566.
Stephens D. C. and Noll K. S. (2006) *Astron. J., 131,* 1142–1148.
Stephens D. C., Noll K. S., and Grundy W. (2004) *IAU Circ. 8289*.
Stern S. A. (2002a) *Astron. J., 124,* 2297–2299.
Stern S. A. (2002b) *Astron. J., 124,* 2300–2304.
Stern S. A., Weaver H. A., Steffl A. J., Mutchler M. J., Merline W. J., et al. (2006) *Nature, 439,* 946–948.
Strazzulla G. (1998) In *Solar System Ices* (B. Schmitt et al., eds.), pp. 281–301. Kluwer, Dordrecht.
Strazzulla G. (2003) *C. R. Physique, 4,* 791–801.
Sykes M. V. (1999) *Icarus, 142,* 155–159.
Sykes M. V. and Walker R. G. (1991) *Science, 251*, 777–780.
Sykes M. V., Cutri R. M., Lebofsky L. A., and Binzel R. P. (1987) *Science, 237,* 1336–1340.
Tedesco E. F., Noah P. V., Noah M., and Price S. D. (2002) *Astron. J., 123,* 1056–1085.
Tegler S. C. and Romanishin W. (1998) *Nature, 392,* 49–51.
Tegler S. C. and Romanishin W. (2000) *Nature, 407,* 979–981.
Tegler S. C. and Romanishin W. (2003) *Icarus, 161,* 181–191.
Tegler S. C., Romanishin W., and Consolmagno G. J. S. J. (2003) *Astrophys. J., 599,* L49–L52.
Thomas N., Eggers S., Ip W.-H., Lichtenberg G., Fitzsimmons A., Jorda L., et al. (2000) *Astrophys. J., 534,* 446–455.
Thébault P. and Doressoundiram A. (2003) *Icarus, 162,* 27–37.
Tholen D. J. (1984) Ph.D. thesis, Univ. of Arizona.
Tholen D. J. and Barucci M. A. (1989) In *Asteroids II* (R. P. Binzel et al., eds.), pp. 298–315. Univ. of Arizona, Tucson.
Tholen D. J. and Buie M. W. (1997) In *Pluto and Charon* (S. A. Stern and D. J. Tholen, eds.), pp. 298–315. Univ. of Arizona, Tucson.
Tran B. N., Ferris J. P., and Chera J. J. (2003) *Icarus, 162,* 114–124.
Trujillo C. A. and Brown M. E. (2002) *Astrophys. J., 566,* L125–L128.
Trujillo C. A., Brown M. E., Rabinowitz D. L., and Geballe T. R. (2005) *Astrophys. J., 627,* 1057–1065.
Veillet C., Parker J. W., Griffin I., Marsden B., Doressoundiram A., et al. (2002) *Nature, 416,* 711–713.
Vilas F. and Gaffey M. J. (1989) *Science, 246,* 790.
Virbiscer A. and Helfenstein P. (1998) In *Solar System Ices* (B. Schmitt et al., eds.), pp. 157–197. Kluwer, Dordrecht.
Weaver H. A., Stern S. A., Mutchler M. J., Steffl A. J., Buie M. W., et al. (2006) *Nature, 439,* 943–945.
Weidenschilling S. J. (2002) *Icarus, 160,* 212–215.
Young E. F., Galdamez K., Buie M. W., Binzel R. P., and Tholen D. J. (1999) *Astron. J., 117,* 1063–1076.